

BRNO UNIVERSITY OF TECHNOLOGY

VYSOKÉ UČENÍ TECHNICKÉ V BRNĚ

CENTRAL EUROPEAN INSTITUTE OF TECHNOLOGY BUT

STŘEDOEVROPSKÝ TECHNOLOGICKÝ INSTITUT VUT

ANALYSIS AND MODIFICATIONS OF 1D NANOSTRUCTURES

ANALÝZA A MODIFIKACE 1D NANOSTRUKTUR

SHORT VERSION OF DOCTORAL THESIS

TEZE DIZERTAČNÍ PRÁCE

AUTHOR Ing. Lukáš Kachtík

AUTOR PRÁCE

SUPERVISOR doc. Ing. Miroslav Kolíbal, Ph.D.

ŠKOLITEL

BRNO 2023

ABSTRACT

The doctoral thesis deals with structural and spectral analysis of 1D nanostructures. First, techniques for the determination of crystallographic structure, as well as spectroscopic ones used to perform this analysis, are introduced with their description and abilities. The following chapter comprises an analysis of multi-walled WS_2 nanotubes using Raman spectroscopy and the process used to count the number of walls in these nanotubes. After that, the most complex chapter follows with the determination of the chirality of the outermost wall of multi-walled WS_2 nanotubes. This chapter also reveals the process of the WS_2 nanotubes growth.

KEYWORDS

1D nanostructures, nanotubes, transmission electron microscopy, Raman spectroscopy, chirality

ABSTRAKT

Tato disertační práce se zabývá strukturální a spektrální analýzou 1D nanostruktur. Nejprve jsou představeny techniky pro určení krystalografické struktury, stejně jako spektroskopické techniky, které byly použity pro tuto analýzu – jejich popis a možnosti. Následující kapitola zahrnuje analýzu vícestěnných WS_2 nanotrubic pomocí Ramanovy spektroskopie a postup, pomocí kterého by bylo možné spočítat počet stěn těchto nanotrubic. Následuje nejobsáhlejší kapitola zaměřující se na určení chirality nejsvrchnější stěny vícestěnné WS_2 nanotrubice, která mimo jiné odhaluje i proces růstu jednotlivých stěn při tvorbě těchto nanotrubic.

KLÍČOVÁ SLOVA

1D nanostruktury, nanotrubice, prozařovací elektronová mikroskopie, Ramanova spektroskopie, chiralita

ACKNOWLEDGEMENT

I would like to give a big thanks to Miroslav Kolíbal, who has been not only my supervisor and mentor but also a great colleague who was a pleasure to work with. Miroslav's motivation and energy kept inspiring me for my whole scientific career, and his support and patience were crucial ingredients in achieving my goals.

Thanks also go to Tomáš Musálek and Tomáš Pejchal for cooperating with them on the nanowire analysis, Kristýna Bukvišová for the TEM discussions, Martin Konečný for the support on the Raman spectrometer, Lukáš Kejík for providing me gold-decorated WS₂ nanotubes, Filip Ligmajer for correlative measurements of the circular dichroism, and to all other colleagues I cooperated with. Special thanks also go to Tomáš Šikola and the Institute of physical engineering staff for creating a friendly environment for all colleagues and students.

CzechNanoLab project LM2018110 funded by MEYS CR is gratefully acknowledged for the financial support of the measurements/sample fabrication at CEITEC Nano Research Infrastructure.

Last but not least, a big thanks also go to my wife, Barbora, who stands with me and supports me in achieving my goals, and to my family for the support and for pushing me by asking 'have you finished yet' again and again.

Contents

ln	trod	uction	1
1	Tec	hniques for spectroscopic and structural analysis	3
	1.1	Transmission electron microscopy	3
	1.2	Raman spectroscopy	5
	1.3	Conclusions	6
2	WS	₂ multi-wall nanotubes – Raman analysis	7
	2.1	Raman analysis of WS_2 nanotubes	7
	2.2	Raman analysis on Witec Alpha 300R	9
	2.3	Conclusions	14
3	Chi	rality determination of the outermost wall of multi-walled \mathbf{WS}_2 nan-	ı
	otu	be	15
	3.1	Chirality in physics	16
	3.2	Chirality-dependent applications of carbon nanotubes	17
	3.3	Chirality-dependent applications of WS_2 and other TMDs nanotubes	17
	3.4	Chirality of nanotubes	18
	3.5	Chirality determination of nanotubes	18
	3.6	Chirality determination of the outermost wall by the chain of nanoparticles	
		on its surface	20
	3.7	Formation of walls	24
	3.8	Conclusions	25
4	Cor	nclusion	27
Li	st of	publications	29
\mathbf{B}^{i}	bliog	graphy	31

Introduction

Nanotechnology has been the era of the past few decades. It has driven the development of new technologies and possibilities to a new level. The reason why all of this is possible is because

"There's Plenty of Room at the Bottom"

– Richard Feynman, Pasadena, 29 December 1959.¹

Nowadays, advanced tools allow us to interact with nanoscale objects – not only to observe the molecules and atoms by various microscopes but also to manipulate with them and even create artificial nanostructures. Modifying and creating nanostructures brings possibilities to develop and manufacture surfaces with a high density of such nanostructures, leading to a high surface-to-volume ratio.

Computer microprocessors have doubled the number of transistors every two years, but these microprocessors' sizes remained unchanged. Being once the size of a room, the extreme scaling allowed modern transistors to fit into a small cellphone. Research in this thesis tries to follow this trend and contribute to it.

For the successful use of semiconductors, their doping is necessary. However, the doping process and the result analysis become difficult when this doping must be performed in nanostructures. Despite that, using semiconductor nanostructures brings properties not seen in bulk, e.g., high-efficient sensors in plasmonics.

Infrared spectroscopy of vibrational molecular resonances is a powerful tool for investigating a wide range of molecules and molecular compounds via their distinct vibrational and rotational absorption resonances, also known as molecular fingerprints [2]. A great effort is now put into overcoming expensive detection techniques in the infrared part of the electromagnetic spectrum (e.g., Fourier Transform Infrared Spectroscopy).

One of the promising possibilities is to use collective excitations of charge carriers in metallic nanostructures, so-called plasmonics. The resonance frequency depends on the nanoparticle's size, geometry, and composition. In the case of standard metals, the resonant frequency lies in the visible-light region, which is not where the molecular fingerprints can be found. To achieve the required response in infrared region by utilizing subwavelength structures, the permittivity needs to be tuned accordingly [3]. One approach is using a heavily doped semiconductor nanostructure, e.g., a nanowire. Knowing the concentration of dopants is essential information about permittivity and, therefore, the vibrational frequency.

Even though WS₂ nanotubes are core parts of the presented research, this thesis does not deal with their growth mechanisms. WS₂ nanotubes were synthesized by Reshef Tenne. The thesis is aimed at analyzing the dependency of Raman spectra on the type

¹More information about Richard Feynman can be found at metamodern.com. His lectures are available at feynmanlectures.caltech.edu. Richard Feynman received a Nobel prize in 1965 [1].

of WS_2 nanostructure, which is a method to simplify the analysis of WS_2 nanotubes by Raman spectroscopy because published experiments are inconsistent. However, the most important topic deals with the analysis of the WS_2 nanotube's structure – its chirality determination, preferably of the outermost wall. Goals are therefore summarized as follows:

- Understand the 1D nanostructures their crystallographic structure and their properties.
- Perform structural and spectral analysis of these nanostructures to achieve the information necessary to understand their growth mechanisms and modification processes.
- Determine the chirality of the outermost wall of the WS_2 nanotube.

To discuss these goals, the thesis is divided into three main chapters. The first chapter describes the structural and spectroscopic tools used to achieve these goals. The second chapter contains Raman analysis of WS₂ nanotubes, and the third chapter contains chirality determination of the WS₂ outermost wall. Each chapter comprises its review, goals, and results. The last chapter summarizes the thesis.

1 Techniques for spectroscopic and structural analysis

This chapter describes techniques used to achieve the required information related to this thesis – mainly structural analysis and vibrational spectra of the structure lattice.

One of the most powerful instruments for nanostructure analysis is a transmission electron microscope equipped with different spectroscopic techniques, offering resolution at the atomic level (section 1.1). An example of information that can be achieved using this tool is information about the crystallographic structure.

A technique entirely different from transmission electron microscopy is Raman spectroscopy. This technique can measure the energies of vibrational states (phonons) in the lattice structure (section 1.2). These three techniques are described in the following sections.

1.1 Transmission electron microscopy

Transmission electron microscopy (TEM, also an abbreviation for Transmission Electron Microscope) is a versatile technique that can perform measurements with atomic resolution. Many imaging modes like bright-field imaging, dark-field imaging, selective area diffraction imaging, scanning bright-field, dark-field, and z-contrast (atomic mass) imaging and their combination allow one to achieve desired information by utilizing only one tool. Moreover, the ability to switch between two main imaging modes, TEM, and STEM (Scanning TEM), on the fly brings TEM usability to an even higher level.

There are several tools like energy-dispersive X-ray spectrometers, energy monochromators, electron energy loss spectrometers, and others that can be attached to the microscope and acquire much more information (primarily analytical).

Almost unlimited information about transmission electron microscopy can be found in [4, 5, 6]. Also, the author's Diploma thesis dealing with transmission electron microscopy may help with questions [7]. In the following sections, only techniques necessary for this thesis are discussed.

TEM imaging (standard imaging mode)

Standard TEM imaging is an easy-to-use technique that allows a moderately skilled operator to perform basic and moderately difficult imaging. It allows us to magnify the image by a few tens to about one million times. Several kinds of images with different information can be acquired in TEM mode. Utilizing these different images helps to resolve many questions related to material structure.

The first mainly used is a bright-field image (BF). This kind of image is well known in most transmission microscopes. Thick parts, where electrons are scattered most, are dark, while parts with thin areas or areas with no sample are bright. Also, heavier elements scatter electrons more than lighter elements, which results in darker parts with heavier

elements and vice versa. This effect also leads to ambiguity where thin areas with heavy elements and thick areas with light elements are present. At first sight, this determination is ambiguous. Contrast in BF imaging can be increased by placing an objective aperture in the diffraction plane such that the primary beam passes through it, while the diffracted and scattered electrons are stopped by the aperture (Fig. 1.1a).

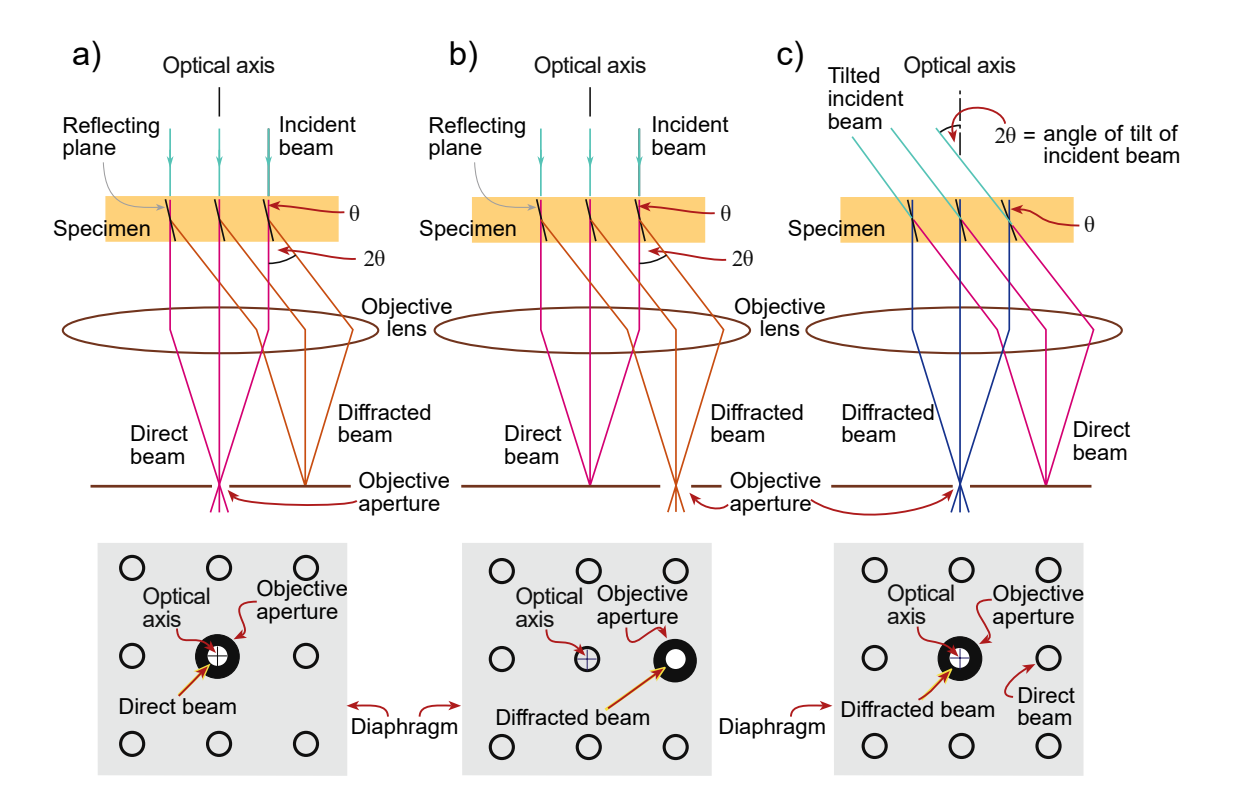


Fig. 1.1: Schematic illustration of a) bright-field image with objective aperture centered around the optic axis; b) dark-field image with aperture centered around the diffracted beam; c) dark-field image with tilted incident beam, which brings the diffracted beam to the optical axis meaning the objective aperture is centered around the diffracted beam and optical axis at the same time. Image adapted from [4] and modified.

Placing the objective aperture off-axis such that the primary beam is stopped creates a dark-field (DF) image (Fig. 1.1b, 1.1c). Compared to BF image, DF image have inverted contrast in general.

The third main type of image is a diffraction pattern. If the incident electron wave before the sample is planar, the diffraction pattern will be located in the back focal plane of the lower objective lens. As was already mentioned, this diffraction pattern is a sum of individual diffraction patterns from areas with the same composition/structure. Identifying these individual diffraction patterns can help determine elements and crystallographic structures (including their orientation).

Scanning transmission electron (STEM) imaging

Most transmission electron microscopes can operate in two completely different imaging modes – the first is the TEM mode (which was described above), and the second is called Scanning transmission electron microscopy (STEM). This mode is like standard scanning electron microscopes (SEM); however, the transmitted electrons are collected. In basic configuration (no aberration correctors), this mode usually has slightly worse resolution than standard TEM mode. Its main advantage is better image interpretation and much higher utilization of analytical tools.

Having a probe at one point in a time (dwell time) is incredibly beneficial for the analytical techniques and understanding the image formation. It allows us to realize that all analytical information comes from a single point in time. As a result, various kinds of maps can be acquired – elemental maps, mapping of plasmon resonance interactions, and others.

1.2 Raman spectroscopy

Raman spectroscopy is a technique with a wide variety of applications. It is highly useful in biological and medical applications – it does not interfere with the water molecules since they have permanent dipole moments [8]. In the DNA double helix, the vibrational states were also observed [9]. Besides that, Raman spectroscopy is widely used in biominerals studies [10]; it is often used in drug analysis and investigation as a tool for gathering evidence [11, 12]. It was already used in several research projects dealing with the detection of explosives from a safe distance (120 m) and for chemical analysis in general [13], and its non-destructivity is an excellent tool for an efficient way to investigate works of art [14]. Typical Raman spectra of WS₂ nanotube can be seen in Fig. 1.2.

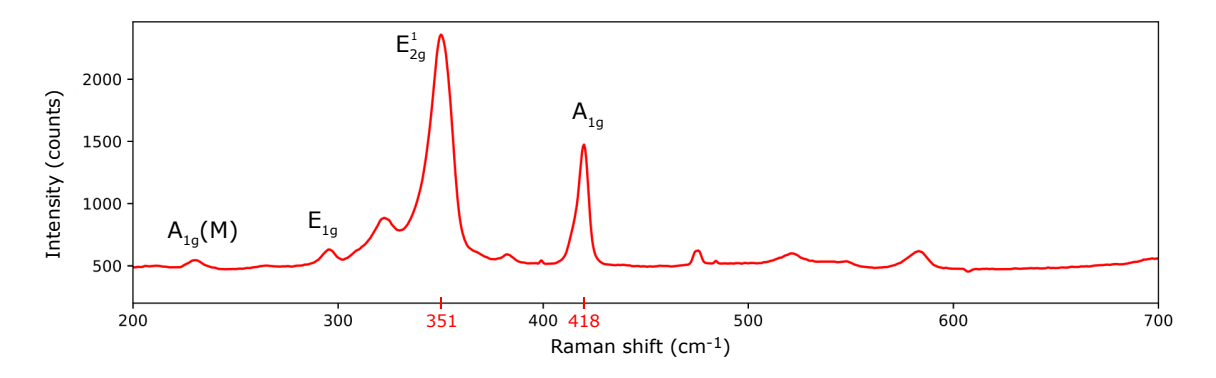


Fig. 1.2: Typical Raman spectra of WS₂ multi-wall nanotube. The two most intense peaks are at positions $351\,\mathrm{cm^{-1}}$ and $418\,\mathrm{cm^{-1}}$. These peaks represent $\mathrm{E^{1}_{2g}}$ and $\mathrm{A_{1g}}$ vibrational modes in the WS₂ structure (see Fig. 2.2). Two other peaks were also identified: $\mathrm{A_{1g}}(\mathrm{M})$ and $\mathrm{E_{1g}}$ at positions $231\,\mathrm{cm^{-1}}$ and $287\,\mathrm{cm^{-1}}$, respectively [15, 16]. Exposure time: $300\,\mathrm{s}$, laser wavelength: $532\,\mathrm{nm}$.

In solid-state physics, Raman spectroscopy is becoming increasingly important in analyzing the optical behavior of nanostructures. This technique can reveal information about the structural, electronic, and optical properties, lattice vibrations, strain, stability, and stacking orders [15].

Raman spectroscopy can also determine the density of stacking faults defects within the InAs nanowire, confirming that Raman spectroscopy is a powerful tool for detecting crystallographic defects [17]. In combination with transmission electron microscopy, Raman spectroscopy can also help to study the crystallographic structure and oxide phases of WS₂ nanotubes [18].

Raman spectroscopy utilizes the inelastic scattering of monochromatic light. For this purpose, a laser beam is used to acquire Raman spectra. When the photon strikes the sample's lattice structure, it interacts with the vibrational states (phonons). This interaction leads to a change in photon energy – either it increases or decreases the energy by the vibrational state's energy. This energy change is described as the Raman shift.

Many factors influence the energy of the phonon. Composition and chemical bonding play a key role. Also, a structure type and its quality can result in slightly different spectra. These changes are specific to the mentioned properties, and studying the Raman spectra can reveal this information.

1.3 Conclusions

In this chapter, we described two crucial techniques for this thesis – TEM imaging and Raman spectroscopy.

In the TEM part, we mentioned fundamental differences between the bright-field and dark-field images. We described how to use the objective aperture and mentioned the diffraction pattern, which is important in structural analysis, as seen in Chapter 3. Another imaging mode – STEM – was also described, including its advantages compared to the standard imaging mode. The most significant difference is that all signals are acquired from a single point in a time. This allows us to use different detectors and analytical tools and create various kinds of maps, like elemental maps.

In the last part, we described a technique entirely different from the previous two – Raman spectroscopy. Various applications were mentioned, showing Raman spectroscopy as a versatile technique.

2 WS₂ multi-wall nanotubes – Raman analysis

WS₂ multi-wall nanotubes are nanotubes composed of more walls. The number of walls affects the nanotube's electrical and mechanical properties, and its knowledge is one of the key information that characterizes their overall properties. There are two approaches to counting the number of walls of the WS₂ multi-wall nanotubes. Either it can be done in a transmission electron microscope or possibly by a Raman spectrometer. The difference between them is that the first approach requires an expensive tool, an expensive tool-time, and the acquisition itself also requires more time.

The dependency of Raman spectra on the number of walls of WS₂ multi-wall nanotubes was already measured [19, 20, 21]; however, these reports are inconsistent [22] (Raman dependency in [19], is opposite compared to the one in [22]). For this reason, it is required to confirm the theory by our measurements and ensure we can measure it correctly using our tools. Understanding the Raman spectra, including this dependency, is also essential to analyze the oxidation states of WS₂ nanotubes. The goal of this part is the following:

• Instead of TEM, use a Raman spectrometer to count the number of walls of the WS₂ multi-wall nanotubes. Clarify the theoretical assumptions and be able to determine the number of walls from the Raman spectrum.

2.1 Raman analysis of WS₂ nanotubes

WS₂ is part of a transition metal dichalcogenides (TMDs) group, where compounds like MoS₂, WS₂, MoSe₂, and WSe₂ belong. These materials follow the success of graphene and have gained extensive attention due to their electronic and optical properties and their broad usage in applications [15]. They exhibit a direct band gap as a monolayer, while bulk structures exhibit an indirect band gap [15, 23, 24].

Atoms in a single layer of TMDs are joined together by covalent bonds while the van der Waals forces keep layers together [15, 25]. This creates interesting physical properties where atoms in a layer are joined together firmly, whereas layers can slide over each other, resulting in a considerable difference between 2D and 3D structures of the same composition. Such behavior also allows us to perform exfoliation of the walls of the multi-layered structures down to a single monolayer [15]. The TMDs' properties can also be tuned by applying external perturbations such as strain, pressure, temperature, or electromagnetic field [15, 26].

WS₂ was the first discovered material to form inorganic nanotubes (INT) in 1992 [27]. Their characteristic properties are high mechanical strength [28, 29], excellent electrical transport properties [30, 31], and thermal stability [32, 33]. They were extensively researched for usage as solid lubricants [34, 35] and nowadays are produced commercially mainly as a lubricant addition [36]. Their lubricating properties are also used in medicine

as self-lubricating coatings for medical insertion devices [37]. Besides their excellent lubricating properties, their addition to the polymer matrix can increase its thermal stability [38, 39]. Mixing WS₂ nanotubes with carbon fibers into the polymer matrix results in a strong synergistic effect [36, 40, 41]. An example of a WS₂ nanotube imaged by TEM is in Fig. 2.1.

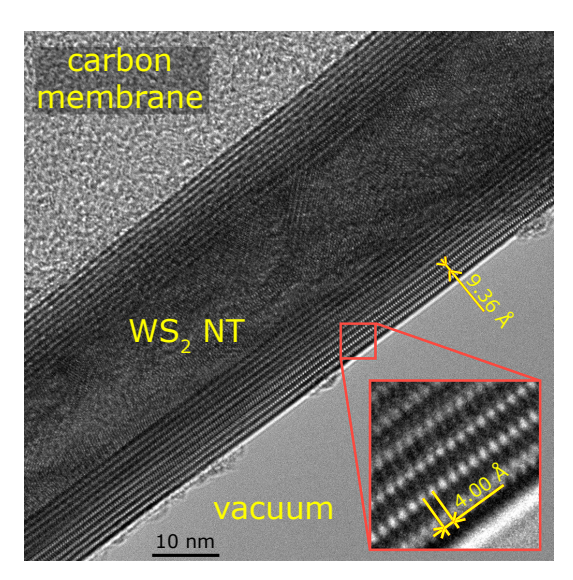


Fig. 2.1: Image of multi-wall WS_2 nanotube from a transmission electron microscope. The nanotube consists of 11 walls. The atomic structure is visible in the bottom right corner.

Properties related to Raman spectroscopy

Some studies discuss Raman spectra dependency on the WS₂ structure type. Intensities and positions of the two most substantial peaks of WS₂ structure near $350 \,\mathrm{cm}^{-1}$ and $420 \,\mathrm{cm}^{-1}$ vary depending on the structure type (WS₂ monolayer, WS₂ few-layer, WS₂ crystal, and WS₂ nanotube) [19, 20, 21]. Also, a strain-induced dependency on Raman spectra was observed (so-called strain-induced phonon shift) [33, 42]. Because laser light is polarized, the dependency of the angle between laser polarization and nanotube direction on the Raman spectra was also studied [43].

Figure 2.2 shows Raman spectra from different WS₂ structures. By looking at the intensities, the A_{1g} peak is much stronger than the E_{2g}^1 peak for nanotube and single crystal than for monolayer and a few-layer structure. Figure 2.2 also shows the atomic displacement in the crystallographic structure. While A_{1g} is out-of-plane atomic displacement, the E_{2g}^1 is in-plane displacement.

According to [16, 19, 42], the A_{1g} mode is weaker for monolayer or few-layer structures because Van der Waals forces are not that significant, and therefore the restoring forces are weaker, causing the vibrations to be less intense. This suggests that the ratio A_{1g}/E_{2g}^1 is dependent on the number of walls in the nanotube and should increase with the increasing number of walls.

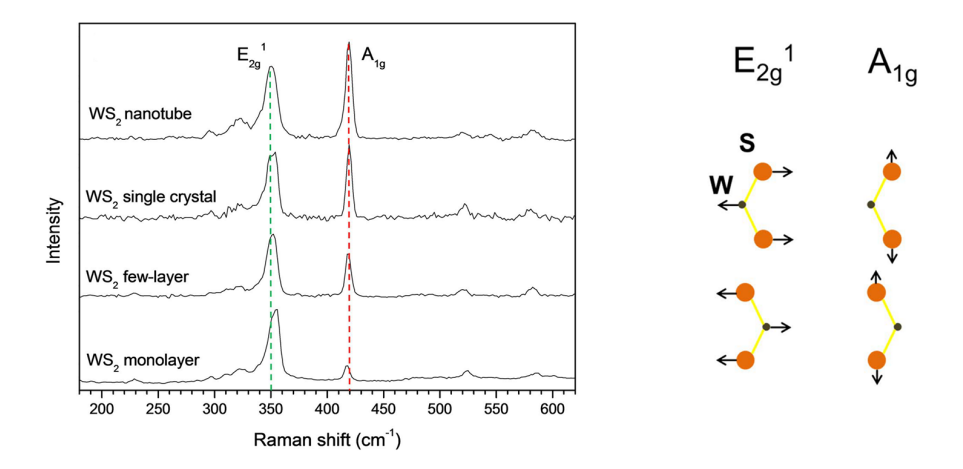


Fig. 2.2: Raman spectra of WS₂ nanotube, WS₂ single crystal, WS₂ few-layered structure, and WS₂ monolayer (left). A clear change in peak intensities and small peak position shifts can be observed. Vibrational modes in Raman 2H structure (right). E_{2g}^1 is the in-plane vibrational mode, and A_{1g} is the out-of-plane vibrational mode. Image adapted from [19] and modified.

2.2 Raman analysis on Witec Alpha 300R

All samples for transmission electron microscope in this thesis were prepared using an isopropyl alcohol (IPA) solution, which was drop cast to a TEM grid. Then, the analysis was performed on a Raman spectrometer *Witec Alpha 300R*. For data processing, a script written in Python was developed.

Experimental setup

The standard experimental setup was the following:

• Laser wavelength: 532 nm

• Objective: Zeiss EC Epiplan-NEOFLUAR DIC 100x (NA: 0.9)

• Exposure time: 300 s

• Diffraction grating: 2400 grids per millimeter

Effect of the experimental setup

In order to minimize the misinterpretation of the results, dependence on laser polarization, exposure time, spectra accumulation, focal plane position, lateral position, and ambient light influence was measured. These results were later used to investigate their possible effect on the measurements. Besides that, different TEM membranes were also tested.

The results are summarized in table 2.1. The most significant influence was caused by polarization adjustment and focal plane position. These two had to be appropriately adjusted before any spectra acquisition (beam polarization was adjusted to the parallel case, and the focal plane was adjusted to the in-focus position). Stage position reproducibility

was not that significant but also not negligible. In this case, not much could be done but using a finer stage movement and positioning the stage as accurately as possible. Other factors were negligible.

Tab. 2.1: Summary of results of all suspected influencing factors.

Factor	Relative std	Significance	
Polarization	N/A	High	
Focal plane position	N/A	High	
Stage position	6.4 %	Medium	
Exposure time	2.8 %	Low	
Accumulation	1.4 %	Low	
Ambient light	N/A	Low	

Experimental procedure

The TEM grid with WS₂ nanotubes was placed into the Raman spectrometer. Then, the correct position and orientation had to be found. Despite utilizing a great Raman's optical microscope, the nanotubes were often too small to be seen. In such scenarios, TEM (or SEM) images were used to help with navigation. The correct laser polarization was derived from the TEM image and the actual Raman image by comparing the sample grid orientations and the target nanotube relative to the grid bar orientation. When this orientation was derived, a correct laser polarization was set.

The correct stage position was found by comparing larger impurities around the target nanotube from the TEM images with the view in the Raman spectrometer. The stage position accuracy was then confirmed by acquiring the spectra. If the spectra exhibited a low signal, the target nanotube was probably missed slightly. In this case, a large area scan was performed to see the position where the spectra are registered. According to the large area scan, the stage position was adjusted to properly fit the target nanotube's position.

As a last step, a correct z-height had to be found. This was done by performing a line scan in the z-direction. Then, the z-position was adjusted according to the maximal signal in the spectra.

Results and discussion

The dependence of the number of walls in nanotube on the A_{1g}/E_{2g}^1 ratio was measured for 34 nanotubes where the number of walls varied from 1 to 43. Three different data sets were used:

• WS₂ nanotubes on carbon membrane (8 nanotubes),

- WS₂ nanotubes on SiN membrane (14 nanotubes),
- WS₂ nanotubes with a tungsten oxide single-crystalline core inside on SiN membrane (13 cases) all data points with one to four walls were these nanotubes with crystalline core inside.

The results of this analysis can be seen in Fig. 2.3. Despite an enormous effort that has been put into neglecting other influencing factors like polarization dependency, focus dependency, and others, the results do not match the theoretical prediction. According to it, the ratio should increase when the number of walls increases. This is not the case.

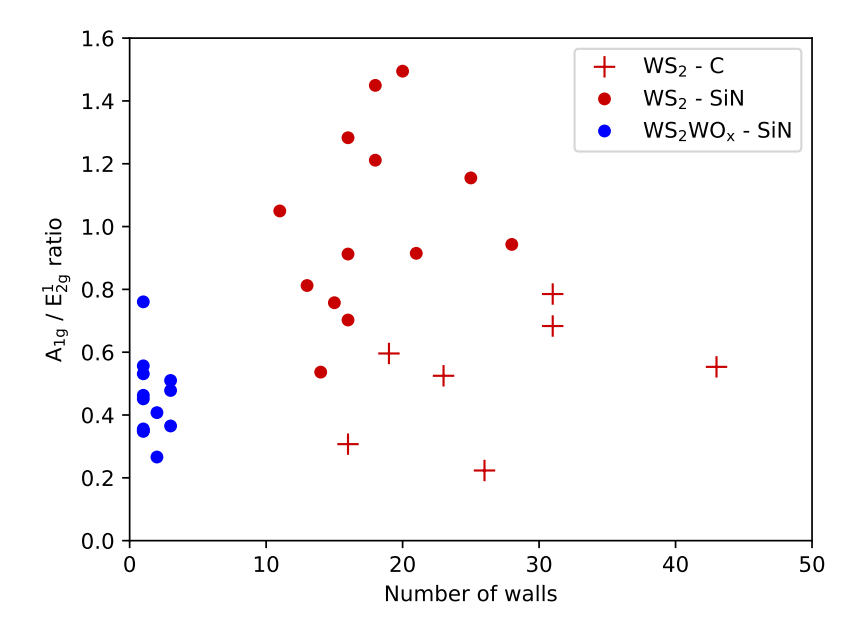


Fig. 2.3: Dependence of A_{1g}/E_{2g}^1 ratio on the number of walls in WS₂ nanotubes. Red marks represent pure WS₂ nanotubes, while blue ones represent WS₂ nanotubes with WO_x core inside. Dots represent nanotubes on the SiN membrane, while crosses represent nanotubes on the carbon membrane. No clear trend is visible within the groups or all of them together. If we compare the results of nanotubes on the SiN membrane, nanotubes with a WO_x core inside have a smaller number of walls, and their overall ratio is smaller (as predicted by the theory), but we cannot exclude that the WO_x core plays a role here. If we compare pure WS₂ nanotubes, those placed on carbon membrane show a lower ratio on average than those on SiN membrane, suggesting that the supporting membrane also influences the results.

Let us divide the results into three parts – nanotubes with tungsten oxide core inside (blue dots), nanotubes on carbon membrane (red crosses), and nanotubes on silicon nitride membrane (red dots).

Nanotubes with tungsten oxide core inside are in the left part of the plot, which is expected since they have only a few walls. We assume the core inside may influence the spectra in terms of a plot as a whole, not within this region. Thus, instead of a core

playing a role here, a strong influence of walls was expected since the relative change is the highest (the absolute number of walls is the lowest). The A_{1g}/E_{2g}^1 ratio values for one, two, and three walls do not show any trend and vary from 0.25 to 0.6 for all three cases. Therefore, no dependence on the number of walls can be seen here.

The other cases without the core are separated according to the used membrane. It shows the Raman spectra depend on the membrane [44, 45]. However, even with this dependency, there is again no clear trend visible neither in the areas together nor within them independently.

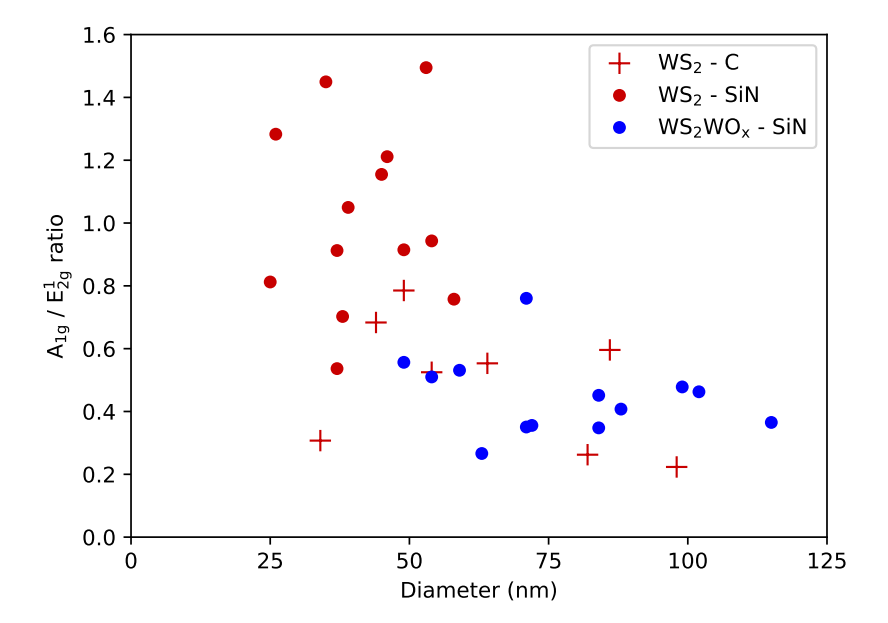


Fig. 2.4: Dependence of A_{1g}/E_{2g}^1 ratio on the diameter of WS₂ nanotubes. Red marks represent WS₂ nanotubes, while blue ones represent WS₂ nanotubes with WO_x core inside. Dots represent nanotubes on the SiN membrane, while crosses represent nanotubes on the carbon membrane. Even though results involve a lot of noise, it can be observed that nanotubes with smaller diameters show a larger ratio. Unfortunately, these results are not conclusive because the data may be influenced by the supporting grid and the WO_x core inside one set of nanotubes.

Dependence of the A_{1g}/E_{2g}^1 ratio on the number of walls is definitely the required output here due to its usage for determining the number of walls by Raman spectrometer; however, no less interesting is the dependence of this ratio on the diameter of the nanotubes. Since the nanotubes with larger diameters usually have more walls (not counting those with a crystalline core inside), this dependency will also be influenced by the number of walls (discussed later). The result of the A_{1g}/E_{2g}^1 ratio on the nanotubes' diameter

can be seen in Fig. 2.4. Even though there is no clear trend, we can see that nanotubes with smaller diameters exhibit a larger A_{1g}/E_{2g}^1 ratio and vice versa. Unfortunately, this cannot be considered a reliable result since the resulting values may be influenced by the supporting membrane and WO_x core inside one set of nanotubes. Furthermore, no clear trend can be observed if we investigate the three groups separately.

The last analysis that can be performed on this data set is the dependency of the number of walls on the diameter. The result can be seen in Fig. 2.5. First, it is important to clarify that this does not involve Raman spectroscopy since all the data in this figure were acquired only in TEM. Moreover, WS₂ nanotubes with WO_x core cannot be considered a representative sample since they are not standard nanotubes. These nanotubes were produced by interrupting the sulfurization process before they were entirely sulfurized [46]. Their number of walls thus depends mainly on the sulfurization process. Because the Raman spectrometer was not involved, both WS₂ nanotubes on carbon and SiN membranes (red ones) are directly comparable and are therefore considered as one group. We can see a weak trend within the pure nanotubes, where a higher number of walls usually means a larger diameter, but it is not always accurate, and the data vary a lot.

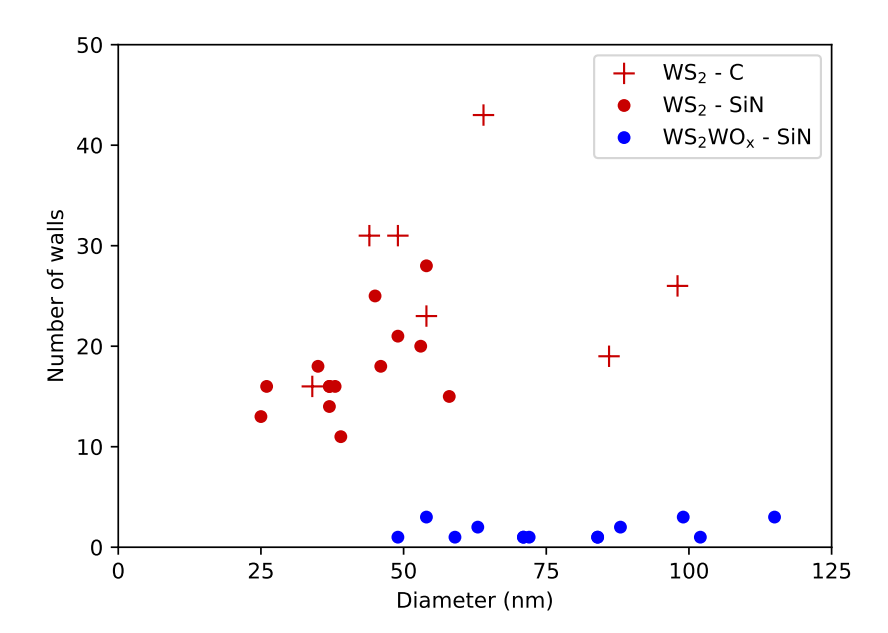


Fig. 2.5: Dependence of the number of walls in WS_2 nanotubes on their diameter. Red marks represent WS_2 nanotubes, while blue ones represent WS_2 nanotubes with WO_x core inside. Dots represent nanotubes on the SiN membrane, while crosses represent nanotubes on the carbon membrane. Pure WS_2 nanotubes show an increasing number of walls with increasing diameters; however, they vary significantly. Nanotubes with WO_x core are also shown for completeness, even though they are not a representative set of samples.

2.3 Conclusions

This chapter described a thorough analysis of WS_2 nanotubes by a Raman spectrometer. First, we explained why the A_{1g}/E_{2g}^1 ratio should depend on the number of walls within the nanotubes. In the following part, results of many 'side effects' that could influence the result dependence were described. The ambient light, the number of accumulations in the acquisition, and the exposure time influenced the results negligibly. The stage position reproducibility was measurable but not much significant. The focal plane position strongly influenced the spectra, and thus the focal plane was always properly focused onto the nanotube by maximizing the intensity of the spectrum. The last test was the dependence on polarization, which turned out to be the strongest factor with respect to Raman peak intensity and ratio. For this reason, a parallel polarization (polarization of laser was parallel to the nanotube's axis) was precisely chosen. Different membranes were also used (carbon and silicon nitride), and different kinds of nanotubes (pure nanotubes and nanotubes with a single-crystalline core inside).

As was already mentioned, the analysis did not show any dependence of the A_{1g}/E_{2g}^1 ratio on the number of walls. The goal of this analysis was to make the determination of the number of walls by Raman spectrometer a cheaper and simpler method compared to the TEM. Not even that we did not confirm this, but we confirmed the exact opposite – the analysis by Raman spectrometer, if ever possible, would be incomparably more complicated and definitely not worth the effort. If we still would like to measure the dependency, no matter how much effort would have to be put into it, there are a few ideas gathered during the measurement we should focus on. Firstly, the analysis should aim to determine how the supporting membrane influences the spectra. Red marks in Fig. 2.3 and 2.4 show the same type of WS₂ nanotubes but on a different membrane. Ideally, they should cover the same area in the plot.

The second factor most likely affecting the results is the purity of the nanotubes and the corresponding purification effect by the heat generated by the laser. We performed a few tests trying to realize the influence of the laser on the WS_2 nanotube, but without much success. We repeatedly acquired the spectra with no changes to the experimental setup and checked how the spectra changed. Unfortunately, we did not observe any clear trend in the changes. We also tried to change the laser power, but no trend of purification was observed. We also tried to see the influence of the purification on the polarization-dependent spectra measurements, and the result showed even weaker dependence and unexpected intensity changes compared to spectra acquired using standard (low) laser power. Even though we did not find any clear trend, we know the laser changes the analyzed environment.

The third factor that could complicate the analysis is that the nanotubes consist of more walls with different chirality. Besides that, we observed many nanotubes in the TEM that did not have a uniform number of walls across their whole length. Even though we tried to choose only the ideal ones or at least large enough parts of the nanotubes with the same number of walls, they were never completely suitable. In conclusion, the quantification of nanotube properties by Raman spectroscopy turned out to be unfeasible.

3 Chirality determination of the outermost wall of multi-walled WS₂ nanotube

Chirality is a geometrical property of objects. Mathematically, chiral objects cannot be superimposed on their mirror image; otherwise, they are called achiral. Examples of such objects can be seen in Fig. 3.1.

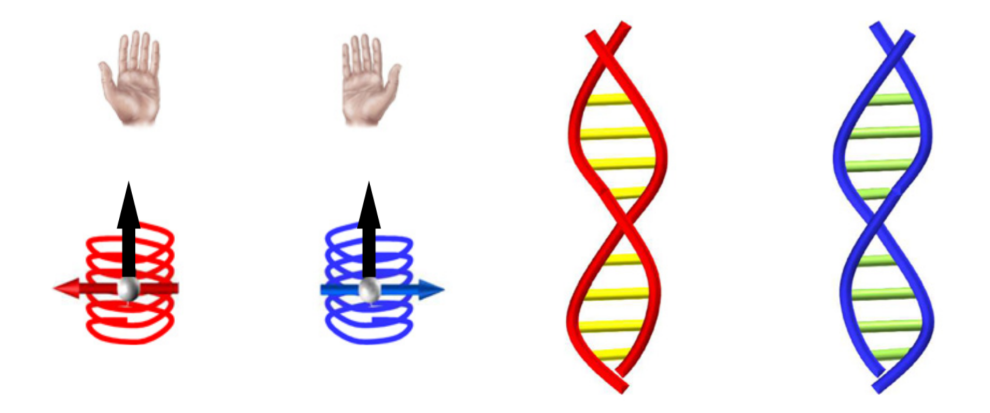


Fig. 3.1: Examples of chiral objects – human hands, electromagnetic waves, and DNA. Image adapted from [47] and modified.

Many kinds of objects exhibit chiral behavior. DNA is one of the most known as its two chains form the double helix. Electromagnetic waves are another example, like circularly polarized light moving within space, where the electric field vector's trajectory creates a helix also. There are also larger and more common objects with a chiral structure. Human hands are one of the most straightforward examples. The left hand is the mirror image of the right hand, and they cannot be superimposed onto each other.

In science, the chirality of objects modifies their behavior. Particularly in chemistry, chirality plays an essential role, e.g., when developing drugs. More than half of the drugs are chiral compounds, and despite the same chemical structure, chiral drugs exhibit differences in biological activities (interaction with proteins, nucleic acids, and others). The differences may be critical – while a drug with one chirality may cure some disease, the same drug with different chirality can even be toxic [48, 49]. In physics, chirality is no less interesting, and the following paragraphs describe it.

The goal of this chapter is to describe techniques that are used to determine the chiral structure of WS₂ nanotubes, what are the advantages, disadvantages, and limitations of these techniques, how they can be combined and presents a new technique that helps to determine the chirality of the outermost wall only, which is essential in many aspects of properties of nanomaterials, like electrical conductivity.

3.1 Chirality in physics

In physics, nanotubes are one of the most common structures to encounter chirality. We can look at the single-wall carbon nanotube (SWCNT) as an example for a better explanation. The SWCNT is created by rolling up the graphene sheet and joining the ends of this sheet together. However, the graphene structure has 6-fold symmetry, which is why it matters how the graphene sheet is rolled up – this is defined by a vector perpendicular to the nanotube's axis. This vector is called chiral vector \mathbf{C} and is defined as

$$\mathbf{C} = n\mathbf{a_1} + m\mathbf{a_2},\tag{3.1}$$

where $n, m \in \mathbb{Z}$ are the indices defining the chirality and $\mathbf{a_1}, \mathbf{a_2}$ are the lattice unit vectors of the graphene sheet, as shown in Fig. 3.2. The chiral vector also defines the chiral angle and the radius of the nanotube.

In general, all nanotubes are chiral except in two important cases where the nanotube is achiral – the zigzag and armchair types. All nanotubes that have a chiral vector (n,0) or (0,m) are zigzag types, and all tubes with a chiral vector (n,n) are armchair types. All other cases are called chiral nanotubes.

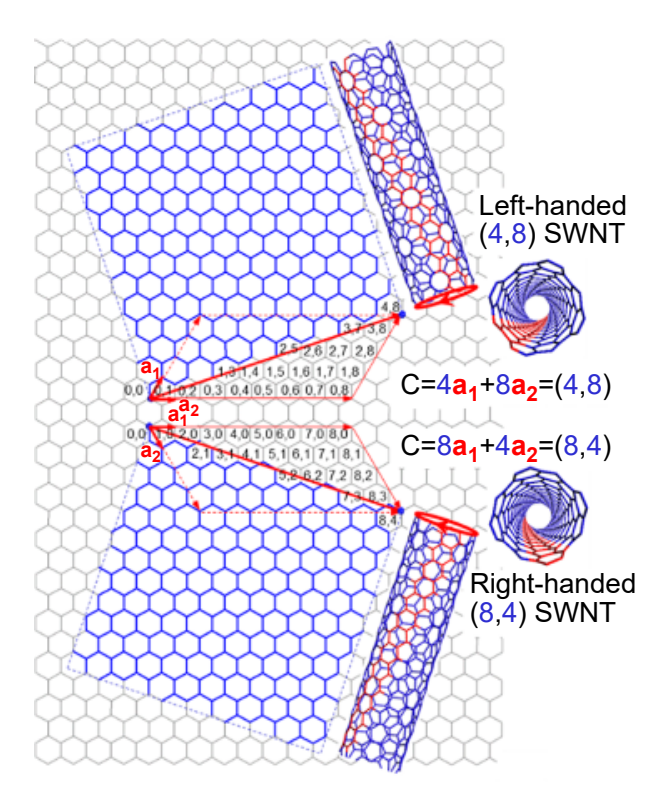


Fig. 3.2: Schematic illustration of rolled-up graphene sheet resulting in a single-wall carbon nanotube. Image adapted from [50] and modified.

3.2 Chirality-dependent applications of carbon nanotubes

Carbon nanotubes are probably the most studied material in connection with chirality. The reasons are apparent – the chirality modifies the nanotube's properties. Furthermore, a carbon nanotube can exist as a single-wall nanotube (SWNT) and a multi-wall nanotube (MWNT), and the wall structure is simple – a rolled-up graphene sheet. These properties make the analysis relatively straightforward.

One of the most studied phenomena is the electrical properties of nanotubes. The significance of carbon nanotubes and their electrical properties are underlined by the TSMC¹, one of the largest companies manufacturing semiconductor devices, which has developed technologies that use carbon nanotubes, allowing it to go beyond the 3 nm manufacturing process [51].

In carbon nanotubes, electrical conductivity is influenced by the nanotube's chirality and radius defined by the chiral vector. While the armchair type is always metallic at room temperature, zigzag and chiral types exhibit either quasi-metallic (with a small band gap) or semiconducting behavior.

3.3 Chirality-dependent applications of WS₂ and other TMDs nanotubes

As was described in previous chapters, chirality directly affects the electrical properties of carbon nanotubes, and WS₂ nanotubes are no exception. WS₂ nanotubes are semi-conducting; thus, they exhibit different band gaps for different structure types. A direct band gap can be observed in the WS₂ monolayer and WS₂ nanotubes with zigzag chirality. On the other hand, an indirect band gap can be found in the WS₂ bulk structure and WS₂ nanotubes with armchair chirality (table 3.1).

Tab. 3.1: Semiconductor types of different WS_2 structures.

Direct band gap	Indirect band gap
WS ₂ monolayer	WS_2 bulk
WS ₂ NT (zigzag)	WS ₂ NT (armchair)

In general, WS₂ nanotubes' electrical resistivity increases exponentially with the increased tensile strength, making the nanotube suitable for piezoresistive strain sensor applications [52]. Regarding the mechanical properties, WS₂ nanotubes are also used as a reinforcing material in different matrices, e.g., increasing the impact resistance while maintaining the elasticity [53]. Similarly, as in carbon nanotubes, WS₂ nanotubes can also be used in nanoelectronics utilizing their chiral-dependent electrical properties.

¹Taiwan Semiconductor Manufacturing Company Limited.

3.4 Chirality of nanotubes

As was already mentioned, chirality is defined by the chiral vector \mathbf{C} , according to equation 3.1. This vector defines the chiral angle θ (which can be derived from a parallelogram) according to the equation

$$\theta = \tan^{-1} \frac{\sqrt{3}m}{2n+m}. (3.2)$$

The chiral angle is dependent only on the m/n ratio and is defined within the range $<0^{\circ}$; $30^{\circ}>$ if the handedness is neglected or within the range $(-30^{\circ}; 30^{\circ}>$ if the handedness is taken into account. In this case, the range $(-30^{\circ}; 0^{\circ})$ defines left-handed chirality while $(0^{\circ}; 30^{\circ})$ defines right-handed chirality. 0° and 30° are achiral cases, where 0° is a zigzag nanotube, and the latter is an armchair nanotube.

Since the chiral vector is defined within the range (-30°; 30°) from the normal vector of the nanotubes axis, its size, together with the angle, also defines the nanotube's perimeter A according to the equation

$$A = a_0 \sqrt{n^2 + m^2 + nm},\tag{3.3}$$

where a_0 is the basis vector, which, in the case of WS₂ structure, is equal to 0.315 nm. The diameter d_t is afterward defined by the equation

$$d_{\rm t} = \frac{A}{\pi} = \frac{a_0}{\pi} \sqrt{n^2 + m^2 + nm}.$$
 (3.4)

The chiral indices n, m, chiral angle θ , and nanotube's diameter d_t are the basis of the nanotube's chirality determination.

3.5 Chirality determination of nanotubes

Techniques used to assign nanotube's chirality are generally classified into optical (spectroscopic) and non-optical techniques. A list of these techniques is in table 3.2.

Tab. 3.2: Summary of optical and non-optical methods for the chirality determination of nanotubes [50].

Optical (spectroscopic) methods Resonant Raman Spectroscopy Photoluminescence Spectroscopy Absorption Spectroscopy Rayleigh Spectroscopy Circular Spectroscopy

Non-optical methods

Scanning Tunneling Microscopy Transmission Electron Microscopy In general, three parameters are used for chirality assignment: Excitonic energy E_{ii} , nanotube's diameter d_t , and the chiral angle θ . Excitonic energy and the nanotube's diameter are used for optical techniques, and the nanotube's diameter and chiral vector are used for non-optical techniques.

Resonant Raman Spectroscopy

Raman spectroscopy is a non-destructive technique extensively used in the chirality assignment of carbon nanotubes. It requires minimal sample preparation – nanotubes can be grown or dispersed on a substrate or dispersed in a solution [50]. Unfortunately, for more complex samples, this method has crucial drawbacks. Often, a Raman spectrometer with a tunable laser is the only option; the sample type should be known beforehand, as well as the supporting membrane type and the surrounding environment. In the end, the accuracy of this method limits the determination, making it often impossible to determine the exact chiral vector [50]. This method becomes too unreliable for multi-wall nanotubes comprising more chiral vectors, so it was not used for chirality assignment in this thesis.

Transmission electron microscopy (TEM)

Transmission electron microscopy is one of the most powerful techniques to acquire atomically resolved images. The d_t value can be measured directly from the image, and in the case of a single-walled nanotube, the θ can be measured from the FFT of the acquired image [50]. Unfortunately, in the case of multi-walled nanotubes, the FFT technique cannot be used to determine the chirality of each wall separately.

More techniques can be utilized for chirality determination. Their limitations vary depending on the required information and used sample – single-wall or multi-wall nanotube, chiral angle or chiral vector, information about the handedness, or knowledge of the chiral angle of the outermost wall of multi-wall nanotube.

One of the techniques is the diffraction pattern. The WS₂ structure forms a hexagonal structure, resulting in a hexagonal-like diffraction pattern. Since one wall is formed by one layer, the diffraction occurs twice on one wall – once on the top and once at the bottom. Thus, one wall creates two hexagonal-line patterns in the diffraction pattern, where their mutual rotation is proportional to the chiral angle. Unfortunately, this method cannot determine the handedness and is suitable for single-wall nanotubes.

A different technique was tested to determine the chirality of the outermost wall. This technique assumes that the outermost wall has the largest surface, and thus the diffraction pattern formed on this wall should be the most intense. For this purpose, a script written in Python was developed. This script calculates the intensities of the diffraction spots from the same wall while considering the beam stopper. Unfortunately, even after applying techniques like image up-scaling for sub-pixel determination and step optimizations, the results did not fully correspond to those measured by other methods. This was most likely caused by the fact that two different walls can have the same chiral angle, resulting in

more intense diffraction peaks than the outermost wall, or that the nanotubes are not perfectly circular, affecting the diffraction intensities as well.

A similar technique based on the largest surface of the outermost wall was tested – dark-field imaging. An objective aperture was used to select only a certain diffraction spot, and since the outermost wall is the largest, the dark-field image of the nanotube should exhibit the largest surface if the correct diffraction spot was selected. Despite this technique being simple, the limitations were in the instrument itself. The smallest objective aperture is not small enough to select only the required diffraction patterns and thus was not usable.

To determine the handedness of the wall, a method utilizing dark-field imaging with a largely tilted beam was tested. The idea comes from the fact that if the electron beam is largely tilted before it impacts the nanotube, the dark-field images from the top and bottom parts should be shifted. Thus, if we select a certain diffraction spot using an objective aperture and acquire an image of the nanotube, we should notice a difference compared to selecting the diffraction spot from another set. Unfortunately, even though the tilt angle was close to 6°, the difference could not be reliably determined.

3.6 Chirality determination of the outermost wall by the chain of nanoparticles on its surface

We described in previous chapters how the chiral angle could be measured – we mentioned the techniques, their limitations, and how these techniques perform when dealing with multi-walled nanotubes. In this chapter, we present a technique that we believe could help determine both the chirality and handedness of the outermost wall of multi-walled nanotubes.

This technique is based on the deposition of different nanoparticles onto the nanotube's surface – the outermost wall. We tried different materials with different results, where the deposition of gold nanoparticles via the liquid solution being the easiest². The deposition was performed by Lukáš Kejík and was done according to [55]. Briefly said, the WS_2 nanotubes were added to a hot $HAuCl_4$ aqueous solution, boiled for some time while stirring, and then cooled down. The dependence of the size of gold nanoparticles on the concentration of WS_2 nanotubes and other parameters are described in [55]. Such a solution with WS_2 -Au nanotubes was then put onto the TEM membrane for further analysis.

As was mentioned in [55], the arrangement of gold nanoparticles is not random and is attributed to surface defects, which results in gold nanoparticles being attached in chains. We utilized this phenomenon, and an example of such a WS₂-Au nanotube is in Fig. 3.3. This nanotube has one long chain of gold nanoparticles. Due to the high energy of electrons

 $^{^2}$ The gold deposition was performed by Lukáš Kejík. Later, a successful deposition of Ge and Ga nanoparticles was performed by Tomáš Musálek [54].

(300 keV) in TEM, the nanotube is transparent, and the chain is visible all around the nanotube, including the opposite side.

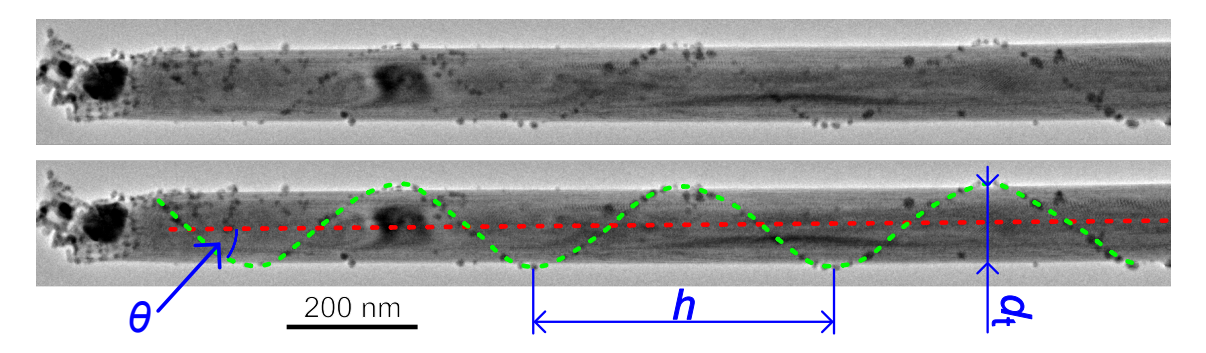


Fig. 3.3: Multiwalled WS₂ nanotube with a gold chain on its surface as imaged in TEM. Top image: label-free image for better observation of gold chain around the nanotube; bottom image: highlighted gold chain (green dashed curve), nanotube's axis (red dashed line), and parameters used for calculation in equation 3.5 (blue).

There are two ways to measure the angle between the gold chain and the nanotube's axis. The first approach is to measure the angle directly from the image. However, this approach assumes that the nanotube is perpendicular to the observer (which in most cases is, since it lies on the membrane), and the angle must be measured at the intersection of the nanotube's axis and the gold chain in the image (where red intersects green in Fig. 3.3). The second approach is to calculate the angle from the knowledge of the nanotube's diameter d_t and the chain periodicity h, as shown in Fig. 3.3. The calculation comes from the fact that if we unroll the gold chain, we receive the right triangle with the length of one leg equal to the h distance and the length of the other leg equal to the πd_t distance. The angle θ can then be calculated from the trigonometry of the right triangle according to equation 3.5

$$\theta = \arctan \frac{\pi d_{\rm t}}{h}.\tag{3.5}$$

It is essential to say that the gold chain in Fig. 3.3 is exceptionally long, and in many cases, the second method will not be accurate since the gold chain may be too short. Therefore, the first method was used in most cases. If the knowledge about handedness is required, it can be achieved by tilting the nanotube and observing the movement of the gold particles – those on the opposite side moves in the opposite direction. If we then know the rotation direction, we can determine the handedness.

Description of the results

All results related to the chirality assignment of the outermost wall are summarized in table 3.3. The first column in the table is the label of the nanotube for a more straightforward discussion. The second and third columns show chiral angles of the outermost wall if the gold chain would be aligned along the zigzag (second column) or armchair (third

Tab. 3.3: Results of chirality analysis of the outermost wall. Image – what would be the chiral angle θ if the gold chain were aligned along the zigzag and armchair direction, respectively. Diffraction – what were all analyzed angles (θ), either manually or by a Python script. The green color within the Image (both zigzag and armchair) and Diffraction – manual columns mean all possible chiral angles found both in the image and diffraction pattern. In the Diffraction – Python (last column), green means the peak with the highest intensity was equal to the zigzag value, red means the peak with the highest intensity was equal to a different value, and yellow means this peak is equal to the zigzag value but was not the highest. All angle values are in degrees.

NI CAID	Ir	nage	Diffraction	
Nr. of NT	zigzag	armchair	manual	Python
			0	1.3
			6	9.3
1	30	0	11	11.2
			15	27.6
			30	29.5
			17	17.4
0	20		25	29.6
2	30	0	29	
			30	
9	16	14	6	14.0
3	15	15	17	16.7
			0	0.5
4	0	22	6	5.5
4	8		17	6.0
			30	7.5
۲	17	13	16	0.1
5	5 17		30	13.9
	12	18	0	8.9
			7	16.3
6			14	17.6
			21	22.3
			30	29.4
7	25	-	16	15.9
1	_ ∠ე	5	23	22.7
8	30	0	30	29.8
9			5	9.0
	21	-9	17	11.5
			21	12.6
			25	16.4
			30	24.7

column) direction. These values were measured directly from the image. The fourth column is all chiral angles manually analyzed from the diffraction patterns. The fifth column is all chiral angles that were analyzed by the script.

Discussion of the results

In table 3.3, we can see that in the case of nanotubes 1, 2, 4, 6, and 9, four or five different chiral angles were found from the manually analyzed diffraction pattern. The rest of the cases involved only one or two different chiral angles. We can also see that each nanotube has one chiral angle in the case of a gold chain in the zigzag direction and one in the armchair direction, except a nanotube 3. This nanotube had two gold chains with entirely different directions, but after the recalculation (rotation by 60°), we found out they showed basically the same direction. However, we noted both angles since they were considered as completely different chains. Also, all of the angles do not involve information about the handedness (thus, all of the angles are determined within the range <0;30>°), except the nanotube 9, which was determined including the handedness in case of Image calculation. This nanotube was therefore determined within the range (-30;30>°.

Looking at the table, we can see that every zigzag value can also be found in manually analyzed diffraction pattern values. In other words, it is possible that all gold chains were aligned along the zigzag direction. Moreover, only one chiral angle was found in nanotube 8, and the gold chain had to be aligned along the zigzag direction (in this case, there was no other option). On the other hand, if we look at the armchair values, we see that only in the case of nanotubes 1 and 3 were the angles also found in manually analyzed diffraction patterns, meaning only in these two cases is the determination ambiguous.

In summary, we can state the following:

- we know for sure that these chains are not aligned along the armchair direction,
- we cannot exclude that they could be aligned along with any random chiral orientation, but it is highly improbable since there was always a match between the image and diffraction value,
- we can state with a high probability that these chains are aligned along the zigzag direction since there was always a match between the zigzag values and diffraction values.

Although we achieved a 100% matching ratio, we admit that there could be a bit of luck and that the gold chains do not have to be aligned along the zigzag direction every time. Unfortunately, we cannot prove this directly – but statistically, it appears that these gold nanoparticles prefer the form along the zigzag direction.

What else can be seen in the table are values that were determined by analyzing the peak intensity in the diffraction pattern using the python script. If we compare these values with the gold-chain values, we notice they are often different. Nanotube 1 did not have

a single most intense peak, but more of them. Still, we can see that angle of 29.5° would match the gold-chain angle if that one would be the most intense. In the case of nanotube 2, the most intense peak was 29°, which matches the gold-chain angle. Nanotube 3 had two peaks with similar diffraction, and both match the gold-chain angle. Nanotube 4 had two of the most intense peaks, whereas only one matched to gold-chain angle. Nanotube 5 did not match the gold-chain angle at all, as well as nanotubes 6 and 7. Nanotube 8 matched the gold-chain angle (which is evident as there was no other option), and the last nanotube 9 did not match the gold-chain angle. We can see that the results are mixed and that we cannot determine the outermost wall's chirality by the most intense peak. However, the automatically processed diffraction pattern has one advantage, which is the precision of the angular determination.

If we put all the information together, we find out that we can determine the chirality of the outermost wall with high accuracy in most cases. The gold nanoparticle chain reveals the chirality of the outermost wall, including its handedness. However, the accuracy is relatively inadequate since the gold nanoparticles are large, and the chains are not so long in most cases. On the other hand, the diffraction pattern can reveal chirality with high accuracy, but it is impossible to determine which chirality belongs to the outermost wall, and we cannot determine the handedness. Thankfully, we can combine this information. We can estimate the chirality according to the gold chains, look at the diffraction pattern and assign the estimated chiral angle to a highly precise chiral angle (preferably processed by the Python script), including the handedness. All of this can be done during a single TEM session. The operator only needs to acquire more images while tilting the nanotube and then acquire the diffraction pattern with high spatial resolution.

3.7 Formation of walls

In the previous section, we described that a chain of gold nanoparticles prefers to attach to the nanotube's surface alongside the armchair direction. However, what makes the gold nanoparticles do that? The answer seems to be the defects. After thoroughly investigating the nanotube's structure in TEM, we observed gold nanoparticles aligned with the wall edges. These edges are visible on the nanotube's side and appear as an additional wall on top of the multi-wall nanotube (Fig. 3.4a).

The nanotube in Fig. 3.4 shows a few exciting things. First, there are edges visible only at the marked positions (A – H). The second fact is that these edges perfectly fit with the chain of gold nanoparticles. The third is that the distance between the edges visualized by the sine curve on the left side has the same periodicity. The fourth exciting feature is that there is always one more wall added when crossing the edge (even in the case F, where there are three more walls, but immediately two walls are 'gone'). The last exciting feature appears when looking at the nanotube from left to right. In the case of the left gold chain, there is always one more wall (never one less). This information suggests that the few outermost walls are not individual walls but one layer twisted into a scroll.

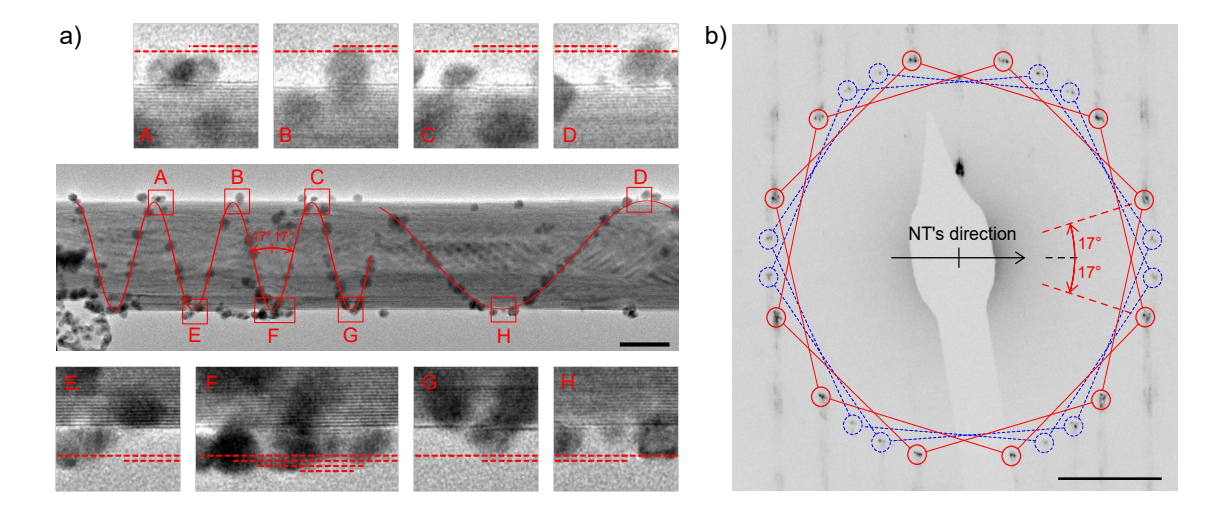


Fig. 3.4: a) The image shows a multi-walled WS₂ nanotube with gold particles on top of it. The gold nanoparticles tend to form a gold-chains around the nanotube. In this case, two gold chains are highlighted by the red sine curves. The nanotube exhibits a structural disorder localized under the gold chains – these disorders can be seen on the edge of the nanotube (A, B, C, D, E, F, G, H cutouts). We can see a single wall that ends at this position in each cutout, highlighted by a red dashed line. If we consider a direction from left to right, we can notice there is always one more single wall in the case of the left-positioned gold chain and one less single wall in the case of the right-positioned gold chain. This means we do not see individual nanotubes but a layer twisted into a scroll (at least for a few outermost 'walls'). The chiral angle of this scroll's edge is 17°. The scroll on the right side is most likely different since it has a different chiral angle. Scale bar: 50 nm; the height of cutouts: 25 nm. b) Image shows a diffraction pattern showing two structures with two different chiral angles. The one highlighted by red hexagons has a chiral angle of 17°, corresponding to the nanotube's left part. Scalebar: 2 nm⁻¹.

3.8 Conclusions

This chapter described in great detail the chirality of nanotubes and how one can measure it. It started with a description of chirality, its definitions, examples, and why chirality matters. It has interesting implications in chemistry, but in physics, chirality is often discussed regarding nanotubes. The chirality of nanotubes modifies the nanotube's properties, e.g., the conductivity. This is being utilized in many applications and is thus essential information.

The chapter then continues with the techniques used to determine the nanotubes' chirality, like Resonant Raman Spectroscopy, and the most important one for us: Transmission Electron Microscopy. Regarding the TEM techniques, an angular measurement from the diffraction pattern, a method based on the most intense diffraction peaks, darkfield imaging, and a beam-tilt-based method were described, including all advantages and disadvantages. In summary, all of these techniques have difficulties when dealing with

multi-walled nanotubes, especially if handedness determination is required.

Then we presented a method based on the deposition of the gold nanoparticles onto the nanotube's surface with promising results. The results showed that we can determine the chiral angle and the handedness of the outermost wall using the gold chains, though the precision of the angular determination is low. But in combination with the diffraction pattern analysis, we can estimate the correct chiral angle of the outermost wall using the gold chain and determine the exact (precise) chiral angle using the diffraction pattern analysis using a Python script. This can be done in the TEM only, using more images of one nanotube. This 'gold chain' method also allows estimating the chiral angle, including the handedness purely in the SEM. This is suitable for applications where nanotubes cannot be placed onto the TEM membrane. The drawback is that the angular resolution is low, and we can see only the gold nanoparticles on top of the nanotube and not those at the bottom.

At the end of this chapter, a process of how the walls are grown on the nanotube was described, using a detailed analysis of defects on the edges of the nanotube. This analysis revealed an interesting fact that the nanotubes are not made of more separate walls but rather a wall that is twisted into a scroll. This analysis also supported the previous results that the position of these defects corresponds to the position of gold chains, confirming that the gold chains are attached along the surface defects. These results were published by the author of this thesis in [54].

4 Conclusion

This doctoral thesis describes the steps that were performed in order to achieve the given goals. First, the techniques for spectroscopic and structural analysis were described in chapter 1. The transmission electron microscopy part described techniques necessary for proper structural analysis – different types of imaging and diffraction patterns acquisition. In the second part, a Raman spectroscopy with its possibilities in general and the details related to this thesis was described.

The second chapter introduced the transition metal dichalcogenides – their structure, properties, applications, and how the Raman spectra should look depending on the number of walls of WS_2 nanotubes. Raman spectra dependency on many different factors was described – laser polarization, exposure time, number of accumulations, the precision of xy- and z-positions, the surrounding illumination, and supporting grid type. Despite an enormous effort to neglect all possible external factors, the results did not show the expected result. The goal was to make it possible to measure the number of walls in WS_2 nanotubes using a Raman spectrometer, but our results showed that the Raman spectrometer is not suitable for this kind of measurement. The resulting dependency was noisy, and no clear trend was observed. We conclude that TEM is still a superior tool for counting the number of walls of WS_2 nanotubes, compared to the analysis by Raman spectrometer.

The last chapter deals with the chirality of WS₂ nanotubes. Several applications relying on the knowledge of chirality were described, including the most common methods for chirality assignment. Those techniques were Resonant Raman spectroscopy, determination by diffraction pattern analysis, direct angle determination using Python script, and the assignment using a dark-field image.

We have introduced a method that can reveal the chirality of the outermost wall. This technique comprises the attachment of gold nanoparticles onto the surface of the WS₂ nanotube. We showed that these gold nanoparticles attach to the zig-zag direction and form a gold chain. The angle of this gold chain then equals the chiral angle. Even though this method can reveal the chirality of the outermost wall, its precision is relatively low. However, in combination with the diffraction pattern analysis, the precision can be, in most cases, increased to about 1°. Moreover, acquiring a tilt series in TEM, or one image in SEM, adds information about the handedness.

Furthermore, a detailed structure analysis also revealed the formation of the outermost walls. It was found that the multi-wall nanotube is not composed of more individual walls but rather one layer twisted into a scroll (at least in the case of the first few outermost walls).

List of publications and other involvements

Journal publications:

- **Kachtík** et al.: Chiral nanoparticle chains on inorganic nanotube templates. (submitted)
- Kolíbal, M.; Bukvišová, K.; **Kachtík, L.**; Zak, A.; Novák, L.; Šikola, T.: Formation of Tungsten Oxide Nanowires by Electron-Beam-Enhanced Oxidation of WS2 Nanotubes and Platelets. Journal of Physical Chemistry C 123 (14) (2019) p. 9552-9559. (https://doi.org/10.1021/acs.jpcc.9b00592)
- Wang, T.; Shi, Y.; Puglisi, F. M.; Chen, S.; Zhu, K.; Zuo, Y.; Li, X.; Jing, X.; Han, T.; Guo, B.; Bukvišová, K.; Kachtík, L.; Kolíbal, M.; Wen, Ch.; Lanza, M.: Electroforming in Metal-Oxide Memristive Synapses. ACS Appl. Mater. Interfaces 12 (2020) p. 11806. (https://doi.org/10.1021/acsami.9b19362)

Oral presentations:

• Kachtík, L.; Musálek, T.; Kolíbal, M.; Šikola, T.: Transmission electron microscopy analysis of 1D nanostructures.

Meeting on TEM in Materials Sciences, 2018, Brno, Czech Republic.

Poster presentations:

- Kachtík, L.; Kejík, L.; Šikola, T.; Kolíbal, M.: Chirality determination of the outermost layer of multi-walled WS2 nanotubes.

 Conference CSMS Microscopy 2020, 2020, Online webinar.
- Kachtík, L.; Musálek, T.; Kolíbal, M.; Šikola, T.: High-resolution transmission electron microscopy analysis of InAs nanowires.
 The 2018 International Conference on Nanoscience + Technology, 2018, Brno, Czech Republic.
- Musálek, T.; Kachtík, L.; Pejchal, T.; Ligmajer, F.; Šikola, T.; Kolíbal, M.: Si dopant incorporation in MBE-grown InAs nanowires
 The 2018 International Conference on Nanoscience + Technology, 2018, Brno, Czech Republic.

- Pejchal, T.; Musálek, T.; Kachtík, L.; Šikola, T.; Kolíbal, M.: Bimetallic catalysts for MBE-grown Ge nanowires
 The 2018 International Conference on Nanoscience + Technology, 2018, Brno, Czech Republic.
- Pejchal, T.; Kachtík, L.; Musálek, T.; Šikola, T.; Kolíbal, M.: Bimetallic catalysts for MBE-grown Ge nanowires
 Nanowire Week 2018, 2018, Hamilton, Canada.
- Musálek, T.; Kachtík, L.; Pejchal, T.; Ligmajer, F.; Šikola, T.; Kolíbal, M.: Si dopant incorporation in MBE-grown InAs nanowires
 Nanowire Week 2018, 2018, Hamilton, Canada.
- Kachtík, L.; Musálek, T.; Kolíbal, M.; Šikola, T.: High-resolution transmission electron microscopy analysis of InAs nanowires.

 Meeting on TEM in Materials Sciences, 2018, Brno, Czech Republic.
- Kachtík, L.; Musálek, T.; Kolíbal, M.; Šikola, T.: High-resolution transmission electron microscopy analysis of InAs nanowires.

 Conference CSMS Microscopy 2018, 2018, Lednice, Czech Republic.

AMISPEC grant:

I have received and successfully defended an AMISPEC grant for the year 2018.

TEM lectures 2018:

After a year of discussion with more than ten people, I have successfully established the cooperation between the Brno University of Technology and Thermo Fisher Scientific (formerly FEI) and incorporated TEM practicum into the laboratory courses at the Institute of physical engineering, Brno University of Technology. I was teaching students to operate TEM in Thermo Fisher Scientific as a part of Advanced Experimental Methods I. These courses continue under the guidance of other lecturers.

Bibliography

- Ρ. [1] R. Feynman, TheDevelopment oftheSpace-Time ViewofQuantumElectrodynamics. Nobel Media AB, Available atnobelprize.org/prizes/physics/1965/feynman/lecture/, 1965.
- [2] F. Huth, A. Govyadinov, S. Amarie, W. Nuansing, F. Keilmann, and R. Hillenbrand, "Nano-FTIR Absorption Spectroscopy of Molecular Fingerprints at 20 nm Spatial Resolution," *Nano Letters*, vol. 12, pp. 3973–3978, Aug. 2012.
- [3] S. Law, L. Yu, A. Rosenberg, and D. Wasserman, "All-Semiconductor Plasmonic Nanoantennas for Infrared Sensing," *Nano Letters*, vol. 13, pp. 4569–4574, Sept. 2013.
- [4] D. B. Williams and C. B. Carter, Transmission electron microscopy: a textbook for materials science. New York: Springer, 2nd ed., 2008.
- [5] L. Reimer and H. Kohl, Transmission electron microscopy: physics of image formation. No. 36 in Springer series in optical sciences, New York, NY: Springer, 5th ed., 2008.
- [6] J. C. H. Spence, High-resolution electron microscopy. Oxford: Oxford University Press, 4th ed., 2013.
- [7] L. Kachtík, Aplikace transmisní elektronové mikroskopie s vysokým rozlišením pro strukturní analýzu nanovláken. Brno: Vysoké učení technické v Brně, Fakulta strojního inženýrství, 2016. 65 p.
- [8] H. J. Butler, L. Ashton, B. Bird, G. Cinque, K. Curtis, J. Dorney, K. Esmonde-White, N. J. Fullwood, B. Gardner, P. L. Martin-Hirsch, M. J. Walsh, M. R. McAinsh, N. Stone, and F. L. Martin, "Using Raman spectroscopy to characterize biological materials," *Nature Protocols*, vol. 11, pp. 664–687, Mar. 2016.
- [9] H. Urabe, Y. Tominaga, and K. Kubota, "Experimental evidence of collective vibrations in DNA double helix (Raman spectroscopy)," The Journal of Chemical Physics, vol. 78, pp. 5937–5939, May 1983.
- [10] P. D. Taylor, O. Vinn, A. Kudryavtsev, and J. W. Schopf, "Raman spectroscopic study of the mineral composition of cirratulid tubes (Annelida, Polychaeta)," *Journal* of Structural Biology, vol. 171, pp. 402–405, Sept. 2010.
- [11] P. V. Huong, "Drug analysis by Raman and micro-Raman spectroscopy," Journal of Pharmaceutical and Biomedical Analysis, vol. 4, pp. 811–823, Jan. 1986.
- [12] C. A. F. de Oliveira Penido, M. T. T. Pacheco, I. K. Lednev, and L. Silveira, "Raman spectroscopy in forensic analysis: identification of cocaine and other illegal drugs of abuse: Raman spectroscopy in forensic toxicology," *Journal of Raman Spectroscopy*, vol. 47, pp. 28–38, Jan. 2016.

- [13] A. K. Misra, S. K. Sharma, T. E. Acosta, J. N. Porter, and D. E. Bates, "Single-Pulse Standoff Raman Detection of Chemicals from 120 m Distance during Daytime," Applied Spectroscopy, vol. 66, pp. 1279–1285, Nov. 2012.
- [14] S. Buckley, "H.G.M. Edwards & J.M. Chalmers (ed.). Raman Spectroscopy in Archaeology and Art History. xxii+476 pages, numerous b&w illustrations, 55 colour plates. 2005. Cambridge: Royal Society of Chemistry; 0-85404-522-8 hardback £130.," Antiquity, vol. 80, pp. 733-734, Sept. 2006.
- [15] X. Zhang, Q.-H. Tan, J.-B. Wu, W. Shi, and P.-H. Tan, "Review on the Raman spectroscopy of different types of layered materials," *Nanoscale*, vol. 8, no. 12, pp. 6435–6450, 2016.
- [16] C. Rice, R. J. Young, R. Zan, U. Bangert, D. Wolverson, T. Georgiou, R. Jalil, and K. S. Novoselov, "Raman-scattering measurements and first-principles calculations of strain-induced phonon shifts in monolayer MoS 2," *Physical Review B*, vol. 87, Feb. 2013.
- [17] R. Tanta, C. Lindberg, S. Lehmann, J. Bolinsson, M. R. Carro-Temboury, K. A. Dick, T. Vosch, T. S. Jespersen, and J. Nygård, "Micro-Raman spectroscopy for the detection of stacking fault density in InAs and GaAs nanowires," *Physical Review B*, vol. 96, Oct. 2017.
- [18] G. Frey, A. Rothschild, J. Sloan, R. Rosentsveig, R. Popovitz-Biro, and R. Tenne, "Investigations of Nonstoichiometric Tungsten Oxide Nanoparticles," *Journal of Solid State Chemistry*, vol. 162, pp. 300–314, Dec. 2001.
- [19] F. Wang, I. A. Kinloch, D. Wolverson, R. Tenne, A. Zak, E. O'Connell, U. Bangert, and R. J. Young, "Strain-induced phonon shifts in tungsten disulfide nanoplatelets and nanotubes," 2D Materials, vol. 4, p. 015007, Oct. 2016.
- [20] M. Viršek, A. Jesih, I. Milošević, M. Damnjanović, and M. Remškar, "Raman scattering of the MoS2 and WS2 single nanotubes," Surface Science, vol. 601, pp. 2868–2872, July 2007.
- [21] M. Krause, M. Virsek, M. Remškar, A. Kolitsch, and W. Möller, "Diameter dependent Raman scattering of WS₂ nanotubes: Diameter dependent Raman scattering of WS₂ nanotubes," physica status solidi (b), vol. 246, pp. 2786–2789, Dec. 2009.
- [22] P. Hajiyev, C. Cong, C. Qiu, and T. Yu, "Contrast and Raman spectroscopy study of single- and few-layered charge density wave material: 2H-TaSe2," *Scientific Reports*, vol. 3, Dec. 2013.
- [23] A. Splendiani, L. Sun, Y. Zhang, T. Li, J. Kim, C.-Y. Chim, G. Galli, and F. Wang, "Emerging Photoluminescence in Monolayer MoS 2," *Nano Letters*, vol. 10, pp. 1271– 1275, Apr. 2010.

- [24] K. F. Mak, C. Lee, J. Hone, J. Shan, and T. F. Heinz, "Atomically Thin MoS 2: A New Direct-Gap Semiconductor," *Physical Review Letters*, vol. 105, Sept. 2010.
- [25] K. Dolui, I. Rungger, C. Das Pemmaraju, and S. Sanvito, "Possible doping strategies for MoS 2 monolayers: An *ab initio* study," *Physical Review B*, vol. 88, Aug. 2013.
- [26] X. Zhang, X.-F. Qiao, W. Shi, J.-B. Wu, D.-S. Jiang, and P.-H. Tan, "Phonon and Raman scattering of two-dimensional transition metal dichalcogenides from monolayer, multilayer to bulk material," *Chemical Society Reviews*, vol. 44, no. 9, pp. 2757–2785, 2015.
- [27] R. Tenne, L. Margulis, M. Genut, and G. Hodes, "Polyhedral and cylindrical structures of tungsten disulphide," *Nature*, vol. 360, pp. 444–446, Dec. 1992.
- [28] I. Kaplan-Ashiri, S. R. Cohen, K. Gartsman, V. Ivanovskaya, T. Heine, G. Seifert, I. Wiesel, H. D. Wagner, and R. Tenne, "On the mechanical behavior of WS2 nanotubes under axial tension and compression," *Proceedings of the National Academy* of Sciences, vol. 103, pp. 523–528, Jan. 2006.
- [29] I. Kaplan-Ashiri and R. Tenne, "Mechanical Properties of WS2 Nanotubes," Journal of Cluster Science, vol. 18, pp. 549–563, Sept. 2007.
- [30] C. Schuffenhauer, G. Wildermuth, J. Felsche, and R. Tenne, "How stable are inorganic fullerene-like particles? Thermal analysis (STA) of inorganic fullerene-like NbS ₂, MoS ₂, and WS ₂ in oxidizing and inert atmospheres in comparison with the bulk material," Phys. Chem. Chem. Phys., vol. 6, no. 15, pp. 3991–4002, 2004.
- [31] C. Zhang, Z. Ning, Y. Liu, T. Xu, Y. Guo, A. Zak, Z. Zhang, S. Wang, R. Tenne, and Q. Chen, "Electrical transport properties of individual WS₂ nanotubes and their dependence on water and oxygen absorption," Applied Physics Letters, vol. 101, p. 113112, Sept. 2012.
- [32] R. Levi, O. Bitton, G. Leitus, R. Tenne, and E. Joselevich, "Field-Effect Transistors Based on WS ₂ Nanotubes with High Current-Carrying Capacity," *Nano Letters*, vol. 13, pp. 3736–3741, Aug. 2013.
- [33] D. Radziuk and H. Möhwald, "Raman scattering from single WS2 nanotubes in stretched PVDF electrospun fibers," *Physical Chemistry Chemical Physics*, vol. 18, no. 1, pp. 21–46, 2016.
- [34] L. Rapoport, Y. Bilik, Y. Feldman, M. Homyonfer, S. R. Cohen, and R. Tenne, "Hollow nanoparticles of WS2 as potential solid-state lubricants," *Nature*, vol. 387, pp. 791–793, June 1997.
- [35] R. Tenne and M. Redlich, "Recent progress in the research of inorganic fullerene-like nanoparticles and inorganic nanotubes," *Chem. Soc. Rev.*, vol. 39, no. 5, pp. 1423– 1434, 2010.

- [36] R. Tenne, "Recent advances in the research of inorganic nanotubes and fullerene-like nanoparticles," *Frontiers of Physics*, vol. 9, pp. 370–377, June 2014.
- [37] A. R. Adini, M. Redlich, and R. Tenne, "Medical applications of inorganic fullerenelike nanoparticles," *Journal of Materials Chemistry*, vol. 21, no. 39, p. 15121, 2011.
- [38] E. Zohar, S. Baruch, M. Shneider, H. Dodiuk, S. Kenig, H. D. Wagner, A. Zak, A. Moshkovith, L. Rapoport, and R. Tenne, "The Mechanical and Tribological Properties of Epoxy Nanocomposites with WS2 Nanotubes," vol. 12, p. 14, 2011.
- [39] M. Naffakh, M. Remškar, C. Marco, and M. A. Gómez-Fatou, "Dynamic Crystal-lization Kinetics and Nucleation Parameters of a New Generation of Nanocomposites Based on Isotactic Polypropylene and MoS ₂ Inorganic Nanotubes," The Journal of Physical Chemistry B, vol. 115, pp. 2850–2856, Mar. 2011.
- [40] A. M. Díez-Pascual, M. Naffakh, C. Marco, and G. Ellis, "Rheological and Tribological Properties of Carbon Nanotube/Thermoplastic Nanocomposites Incorporating Inorganic Fullerene-Like WS₂ Nanoparticles," The Journal of Physical Chemistry B, vol. 116, pp. 7959–7969, July 2012.
- [41] A. M. Díez-Pascual, M. Naffakh, C. Marco, and G. Ellis, "Mechanical and electrical properties of carbon nanotube/poly(phenylene sulphide) composites incorporating polyetherimide and inorganic fullerene-like nanoparticles," *Composites Part A: Applied Science and Manufacturing*, vol. 43, pp. 603–612, Apr. 2012.
- [42] X. H. Wang, C. C. Zheng, and J. Q. Ning, "Influence of curvature strain and Van der Waals force on the inter-layer vibration mode of WS2 nanotubes: A confocal micro-Raman spectroscopic study," *Scientific Reports*, vol. 6, Dec. 2016.
- [43] K. Gartsman, "Micro Raman Investigation of WS2 Nanotubes," vol. 786, pp. 349–352, AIP, 2005.
- [44] D. Zhang, Y.-C. Wu, M. Yang, X. Liu, C. O. Coileáin, M. Abid, M. Abid, J.-J. Wang, I. Shvets, H. Xu, B. S. Chun, H. Liu, and H.-C. Wu, "Surface enhanced Raman scattering of monolayer MX2 with metallic nano particles," *Scientific Reports*, vol. 6, p. 30320, July 2016.
- [45] S. A. Ghopry, M. A. Alamri, R. Goul, R. Sakidja, and J. Z. Wu, "Extraordinary Sensitivity of Surface-Enhanced Raman Spectroscopy of Molecules on MoS₂ (WS₂) Nanodomes/Graphene van der Waals Heterostructure Substrates," Advanced Optical Materials, vol. 7, p. 1801249, Apr. 2019.
- [46] P. Chithaiah, S. Ghosh, A. Idelevich, L. Rovinsky, T. Livneh, and A. Zak, "Solving the "MoS₂ Nanotubes" Synthetic Enigma and Elucidating the Route for Their Catalyst-Free and Scalable Production," ACS Nano, vol. 14, pp. 3004–3016, Mar. 2020.

- [47] S.-H. Yang, "Spintronics on chiral objects," Applied Physics Letters, vol. 116, p. 120502, Mar. 2020.
- [48] N. Ananthi, "Role of Chirality in Drugs," Organic & Medicinal Chemistry International Journal, vol. 5, Feb. 2018.
- [49] W. H. Brooks, W. C. Guida, and K. G. Daniel, "The Significance of Chirality in Drug Design and Development," Current Topics in Medicinal Chemistry, vol. 11, pp. 760–770, Apr. 2011.
- [50] F. Yang, M. Wang, D. Zhang, J. Yang, M. Zheng, and Y. Li, "Chirality Pure Carbon Nanotubes: Growth, Sorting, and Characterization," *Chemical Reviews*, vol. 120, pp. 2693–2758, Mar. 2020.
- [51] "TSMC to Start Mass Production of 3nm Chips in 2022." CNX SOFTWARE EMBEDDED SYSTEMS NEWS [online]. Hong Kong: Aufranc, 2020 [cit. 2020-11-09]. Available from: https://www.cnx-software.com/2020/08/29/tsmc-to-start-mass-production-of-3nm-chips-in-2022/.
- [52] A. Grillo, M. Passacantando, A. Zak, A. Pelella, and A. Di Bartolomeo, "WS 2 Nanotubes: Electrical Conduction and Field Emission Under Electron Irradiation and Mechanical Stress," Small, vol. 16, p. 2002880, Sept. 2020.
- [53] S. Ghosh, G. Otorgust, A. Idelevich, O. Regev, I. Lapsker, D. Y. Lewitus, and A. Zak, "Reinforcement of poly (methyl methacrylate) by WS2 nanotubes towards antiballistic applications," *Composites Science and Technology*, vol. 207, p. 108736, May 2021.
- [54] Kachtík et al., "Chiral nanoparticle chains on inorganic nanotube templates," (sub-mitted).
- [55] A. Y. Polyakov, L. Yadgarov, R. Popovitz-Biro, V. A. Lebedev, I. Pinkas, R. Rosentsveig, Y. Feldman, A. E. Goldt, E. A. Goodilin, and R. Tenne, "Decoration of WS₂ Nanotubes and Fullerene-Like MoS₂ with Gold Nanoparticles," *The Journal of Physical Chemistry C*, vol. 118, pp. 2161–2169, Jan. 2014.